Journal of Materials Chemistry A

Accepted Manuscript

ROYAL SOCIETY OF CHEMISTRY

www.rsc.org/materialsA

RSC Publishing

Paper

Surface zwitterionic functionalized graphene oxide for a novel loose nanofiltration membrane

Junyong Zhu [a], Miaomiao Tian [a], Jingwei Hou [b], Jing Wang [a], Jiuyang Lin [c], Yatao Zhang [a*], Jindun Liu [a], Bart Van der Bruggen [c]

Received
Accepted

www.rsc.org/

Surface zwitterionization of graphene oxide (GO) was firstly synthesized by grafting poly (sulfobetaine methacrylate) (PSBMA) onto the GO surface *via* reverse atom transfer radical polymerization (RATRP). Then, a novel type of GO-PSBMA/polyethersulfone (PES) loose nanofiltration membrane (NFM) was constructed by mixing with modified GO composites *via* phase inversion. FTIR, XRD, TEM, XPS and TGA were applied to analyze the chemical composition and morphology, confirming a favorable synthesis of GO-PSBMA composites. Besides, the effect of the embedded GO-PSBMA nanoplates on the morphology and overall performance of the hybrid membranes was systematically investigated based on the SEM images, water contact angle, zeta potential, and fouling parameters. It was found that water flux of hybrid membrane was greatly enhanced from 6.44 L m^{-2} h^{-1} bar^{-1} to 11.98 L m^{-2} h^{-1} bar^{-1} when the GO-PSBMA content increased from 0 to 0.22 wt%. The antifouling tests revealed that GO-PSBMA embedded membranes have an excellent antifouling performance: a high flux recovery ratio (ca. 94.4%) and a low total flux decline ratio (ca. 0.18). Additionally, the hybrid membranes exhibited a distinct advance in mechanical strength due to the addition of highly rigid GO. Notably, compared with unmodified membrane, the hybrid membranes had a higher retention of Reactive Black 5 (99.2%) and Reactive Red 49 (97.2%), and a lower rejection of bivalent salts (10% for Na_2SO_4) at an operational pressure of 0.4 MPa, rendering the membranes promising for dye/salt fractionation.

Introduction

A growing volume of reactive dyes are broadly applied in various fields, such as dyeing and printing, thus generating a mass of dye wastewater which causes a considerable environmental pollution and serious health hazards [1-3]. Commonly, inorganic salts involving NaCl (~6.0 wt.%) and Na_2SO_4 (~5.6 wt.%) are added to enhance dye pickup of the targets in dyeing process[4]. Besides, in the process of dye synthesis, a large amount of inorganic salts (mainly NaCl), intermediates with low molecular weight, and residual compounds are concomitantly generated, inevitably impairing the stability and quality of dye products[5]. Overall, the high concentration of salts existing in dyes wastewater not only limits the biodegradation of organic solutes by microorganisms, but also complicates conventional physico-chemical treatment processes, such as adsorption and chemical degradation, rendering dye/salt mixtures difficult to be treat and separate[6, 7]. In the concept of sustainability, the treatment of textile wastewater urgently requires a new paradigm shift to emphasize on resource recovery (both salts and dyes) from wastewater instead of dye removal or pure water production by classical filtration, e.g., reverse osmosis. Above all, the fractionation of dye/salt mixtures has been increasingly crucial in view of dye desalination, reuse and purification both in the dye synthesis and dyeing procedures.

Nanofiltration (NF) has been demonstrated as a competitive alternative for the treatment of textile wastewater due to ease of operation and control, low initial investment and consumption energy and feasible recovery of valuable dyes[8-14]. Low molecular weight (LMW) uncharged solutes are rejected mainly by steric hindrance (exclusion effect), whereas charged solutes (especially for multivalent salts) are retained primarily by electrostatic interactions (Donnan effect). Recently, two types of loose NF membranes (Sepro NF 6 and NF 2A, Ultura) were applied by Lin *et al.*[15] for the fractionation of direct dye/salt mixtures. The results showed that both membranes retained more than 99.6% direct dyes (i.e., direct red 80, direct red 23, and Congo red) with 98% permeation of NaCl, indicating that loose NF membranes have potential for dye/salt fractionation. Yu *et al.*[16] fabricated positively charged loose NF membrane (HNTs-PIL/PES and SiO_2-PIL/PES membrane) via the blending-phase inversion method. The combination of a loose structure and high surface charge density promoted salts (NaCl and Na_2SO_4) permeation to a great extent.

Polyethersulfone (PES) is an ideal polymer material for the design of membrane, mainly due to its good thermal stability, superior pH and chlorine tolerance, as well as excellent chemical resistance[17-19]. Nonetheless, a further application of pristine PES membranes in water treatment is hindered due to severe fouling ascribed to its intrinsic hydrophobicity, which could result in a sharp decline of

permeability and lifespan. Recently, considerable attempts have been made to develop advanced composite polymeric membranes for improving antifouling and permselectivity performance[20, 21]. Thin-film composite (TFC) membranes are mainly fabricated *via* interfacial polymerization (IP)[22-24], which is an effective way to construct the dense NF membranes. However, the type of TFC membranes with a high surface charge and dense active layer generally has a high retention of multi-valent salts, which makes them unsuitable for the fractionation of dye/salt mixtures. In addition, Van der Bruggen *et al.*[25] demonstrated that a high osmotic pressure induced by the high rejection of commercially available dense NF membranes has a negative influence on the membrane flux during the treatment of textile wastewater. On the contrary, loose NF membrane[26-29] with larger pore size enable salts to permeate, which alleviates the osmotic pressure difference across the membrane and the concentration polarization of salts and thus facilitates the peremation flux. Therefore, in the treatment of textile wastewater, a dedicated NFM with an effective separation of dye/salt mixture is required. In addition, the compatibility and adhesion between the active layer and substrate are often poor, leading to the detachment of the skin layer from the substrate when applied in harsh environments for a long time. Many other modifications like surface graft polymerization[30], dip-coating[31] and crosslinking[32] may possibly improve the adhesion and compatibility due to the formation of a stable chemical bond with the adhesive layer. However, such synthesis methods consisting of many complicated steps are difficult to control and unfriendly to the environment. Consequently, a facile route of incorporating nanofillers (i.e., metal-organic frameworks, halloysite nanotubes, TiO_2, carbon nanotubes, and montmorillonite) into the polymeric matrix to construct hybrid membranes has stimulated a vast amount of research in recent years[33-37]. The mixing of inorganic nanoparticles in the polymer matrix can improve surface hydrophilicity, mechanical properties, water permeability and the antifouling performance of polymer-based composite membranes.

Graphene oxide (GO) comprising a range of reactive oxygen functional groups (epoxide, hydroxyl, carbonyl, and carboxyl groups) has represented a desired alternative for designing the hybrid membranes due to its peculiar 2D nanoplate structure, large specific surface area, good mechanical properties, and strong hydrophilicity[38-40]. Pristine GO has been embedded into the polymer matrix to design advanced membranes with enhanced permeation flux and antifouling performance[41, 42]. However, graphene derivates are prone to aggregation in the dope solution, forming a random dispersion which may cause partial flaw through the membranes. In addition, the compatibility and adhesion force between GO and the polymer are poor, giving rise to the concomitant defect interface which would deteriorate the permselectivity and mechanical properties of composite membranes[42, 43]. Therefore, the modification of GO for the optimized compatibility and improved overall performance is indispensable. Zwitterionic polymers including phosphobetaine, carboxybetaine, sulfobetaine, bearing both anionic and cationic groups in the same monomer unit, were observed to have an excellent anti-biofouling performance[44-47]. Recently, Ye *et al.* reported a dual functional block copolymer brushes on TFC membranes for anti-biofouling [48]. Zwitterionic polymers were used to endow membrane surface with strong hadration capacity and low fouling propensity. Liu *et al.* constructed the ion-responsive memrbane with zwitterion-carbon nanotube (ZCNT) entrances at the surface via IP. Poly(sulfobetaine) brushes could be used as gatekeepers at the tip of CNTs due to the ion-responsiveness of zwitterionic chains, whose confugration could be finetuned by the ionic strength, thus forming a ultrahigh mono-/multivalent ion selectivity [49]. Zwitterionic polymers with hydrophilic groups form a hydration layer *via* electrostatic interaction and hydrogen bond, which can efficiently promote the permeability and antifouling performance. Besides, the hydrophobic chains in zwitterionic polymers are well miscible with polymer matrix. Thus, a zwitterionic polymer can also optimize the compatibility between the modified inorganic nanofillers and the polymer matrix.

In this work, GO bearing poly (sulfobetaine methacrylate) brush (GO-PSBMA) was synthesized *via* RATRP. Then loose NF membranes were prepared by mixing GO-PSBMA composites with PES material *via* phase inversion. The effects of nanocomposites on the membrane surface hydrophilicity, microstructure and surface charge were investigated. In addition, we also studied the influences of GO-PSBMA content on the separation, antifouling and mechanical performance of hybrid membranes. The rejection of loose NF membranes in a single-component (i.e., NaCl or reactive dyes) solution was studied at variable pressures.

Experimental

Materials

Natural graphite powders (45 μm) were purchased from Sinopharm Chemical Reagent, China. Polyethersulfone (PES, *Mw*=55,000 Da) was obtained from BASF. N-dimethylacetamide (DMAc) and polyvinylpyrrolidone (PVP, *Mw*=24,000 Da) were purchased from Tianjin Kewei Chemical Reagent Co. Ltd., China. Bovine serum albumin (BSA) was purchased from Sigma-Aldrich. Reactive Red 49 (*Mw*=576.49 Da) and Reactive Black 5 (*Mw*=991.82 Da) were obtained from Sunwell Chemicals Co. Ltd., China; the structural formulas are reported elsewhere [2,11]. Sulfobetaine methacrylate (SBMA), 2-bromoisobutyryl bromide (BIBB), 3-aminopropyl triethoxysilane (APTES), triethylamine (TEA) and 2, 2'-bipyridine (bpy), azodiisobutyronitrile (AIBN) were purchased from Aldrich Chemical Co. and used as received. All the other chemicals (analytical grade) were obtained from Tianjin Kermel Chemical Reagent Co., Ltd., China and used as received. Deionized water was used throughout in this work.

Preparation of PSBMA brushes modified Graphene oxide

The procedures and reaction schemes for the preparation of GO and GO-PSBMA are shown in Fig. 1. The detailed synthesis of GO, BTPAm and initiator anchoring on GO surface are shown in supplementary information (S1-S3).

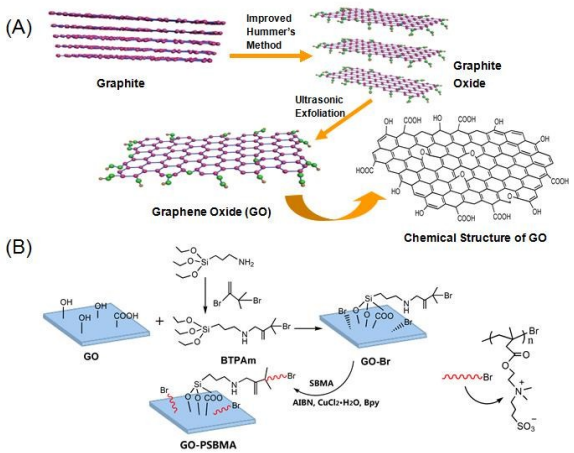

Fig. 1 Preparation process of (A) GO, (B) GO-PSBMA composites

Polymerization of PSBMA onto GO-Br *via* RATRP

The mixture of initiator-modified GO-Br (200 mg), SBMA monomer (1.5 mmol), methanol (30 mL) and water (10 mL) was introduced in the flask. Then AIBN (20 mg) dissolved in methanol (10 mL) was added into the mixture. The flask was purged by vacuum and back-flushed with nitrogen three times, and then left under nitrogen atmosphere. Subsequently, 2, 2'-bipyridine (0.16 mmol) and $CuCl_2 \cdot 2H_2O$ (0.32 mmol) dispersed in methanol (10 mL) were added into the mixture. RATRP reactions were performed in a 100 mL four-neck flask in an oil-bath at 65°C for 10 h under a nitrogen atmosphere. Finally GO-PSBMA nanocomposites were obtained by centrifugation with washing by methanol and then dried in a vacuum oven at 40°C.

Preparation of GO-PSBMA nanocomposites embedded nanofiltration membrane

Asymmetric flat sheet PES membranes containing GO-PSBMA composites were fabricated by phase inversion induced by the immersion precipitation technique. The casting solutions were prepared to achieve final content of PES (22.0 wt.%), PVP (1.0 wt.%) and DMAc with different content of HNTs-poly(NASS) composites (0, 0.11 wt.%, 0.22 wt.% and 0.44 wt.%). Firstly, a certain amount of GO-PSBMA was well dispersed into DMAc with ultrasonic treatment for 10 min. Then the uniform suspension was mixed with PES and PVP under continuous stirring at room temperature for 12 h. After degasification, the homogeneous solution was cast on a glass substrate by a casting knife with 0.1 mm thickness, and subsequently immersed into a coagulation bath (deionized water, 22°C) for precipitation. Finally the resulting membranes were kept in deionized water, which was replaced every day. Membranes prepared with different GO-PSBMA content of 0, 0.11, 0.22 and 0.44 wt.% in the dope solution are further referred to as NFM-0, NFM-1, NFM-2 and NFM-3, respectively.

Characterization of the GO-PSBMA nanocomposite

Fourier transform-infrared spectroscopy (FT-IR)

The chemical compositions of GO, BTPAm, GO-Br and GO-PSBMA were measured on a FT-IR Thermo Nicolet IR 200 spectroscope (Thermo Nicolet Corporation, USA) in the range of 4000-400 cm^{-1}. Each spectrum was captured by 64 scans at a resolution of 2 cm^{-1} using KBr pellets.

Thermogravimetric analysis (TGA)

TGA measurements were carried out using a TG-DTA, DT-40 system (Shimadzu, Japan). Samples (5 mg) were heated from room temperature to 800°C at 10°C/min in the nitrogen atmosphere under a flow of nitrogen.

X-ray diffraction (XRD)

X-ray diffraction (XRD) patterns of the sheet samples (GO, GO-Br and GO-PSBMA) were recorded by PANalytical X' Pert Pro (PANalytical, Netherlands) in the scanning range of 4° and 15° with area detector operating at a voltage of 40 kV and a current of 40 mA using copper *Kα* radiation. GO, GO-Br and GO-PSBMA were tested as powders.

Transmission electron microscopy (TEM)

The powders (GO and GO-PSBMA) were evenly dispersed in ethanol solution, then the suspended particles were transferred to a copper grid (400 meshes) coated with a strong carbon film. The samples were investigated by a FEI Tecnai G^2 transmission electron microscope (JEOL JEM 2100F) under 200 kV acceleration voltages.

X-ray photoelectron spectroscopy (XPS)

For the XPS analysis, the base pressure of the analyzer chamber was about 5×10^{-7} Pa. The survey spectra (from 0 to 1400 eV) were recorded. During the wide-scan, peak for C 1s was observed at binding energy 284.7 eV. All readings were calibrated with the corresponding C 1s as the standard for the correction of charging effects.

Characterization of NF membrane

Scanning electron microscopy (SEM)

The samples were washed by deionized water and dried at room temperature, then fractured in liquid nitrogen. Cross-sections of the membranes were sputtered with gold, which were observed with the microscope at 10 kV. The structure of the membranes was inspected by SEM using a JEOL model JSM-670 0F scanning electron microscope (JEOL, Japan).

Dynamic contact angle (DCA)

The water contact angle of the membrane was operated on a contact angle goniometer (OCA20, Dataphysics Instruments, and Germany) at room temperature and 50% relative humidity. All contact angle measurements were made using 2 μL of deionized water. To make the contact angle more persuasive, the contact angle was measured at five random locations for each sample (5cm × 1cm) and the average was determined.

Water uptake

The as-prepared samples (1 g) were dried under vacuum at 30°C till constant weight and then immersed in water for 24 h. After that, the weight of wet membranes, whose surface was mopped using the blotting paper, was noted down. Finally the membranes were completely dried anew under vacuum at 30°C. The water uptake (W_u) can be calculated by the following equation:

$$Wu = \frac{m_1 - m_2}{m_2} \times 100\% \quad (1)$$

Where m_1 is the weight of wet membrane after dried by blotting paper, m_2 is the weight of the complete dried membrane.

Porosity

The porosity (ε) was determined by gravimetric method, as defined in the following equation [51, 52]:

$$\varepsilon = \frac{(m_1 - m_2)/\rho_1}{(m_1 - m_2)/\rho_1 + m_2/\rho_2} \quad (2)$$

Where m_1 is the weight of the wet membrane; m_2 is the weight of the dry membrane; ρ_1 is water density at 25°C and ρ_2 is the density of PES.

Charge property of NF membrane

The charge property of NFMs surface was characterized by the zeta potential, which was measured with a streaming current method on an electrokinetic analyzer (Surpass Anton Paar, Austria). The area of each sample was 0.2 cm × 0.1 cm and the selected flat membranes were immobilized to the adjustable gap cell. KCl solution (1.0 mmol/L) was used for the determination of the zeta potentials, which were measured at various pH values. Hydrochloric acid (HCl) and potassium hydroxide (KOH) were used to adjust the pH. The measurement progress was controlled by the software (Visolab for Surpass).

Nanofiltration performance test

NF performance of the as-prepared membranes was investigated with a cross-flow module at 25°C in the range of 0.2-0.8 MPa. The membranes were pressurized with deionized water at 0.8 MPa to reach a steady state before testing. The detailed operation of the NF setup was described elsewhere [53]. After the compaction, the pure water flux was recorded at ambient temperature at different pressures. Salt (NaCl, $MgCl_2$, Na_2SO_4 and $MgSO_4$, 1 g L^{-1}) rejection were measured at 0.4 MPa with flow velocity of 40 L h^{-1}. In addition, RR49 and RB5 rejection, separately, were measured at the same conditions as the salt rejection experiment, and at a concentration of 0.5 g L^{-1}. The permeation flux (J) and rejection (R) was calculated using the following equations:

$$J = \frac{V}{A \times \Delta t} \quad (3)$$

$$R = \frac{C_f - C_p}{C_f} \quad (4)$$

where V is the volume of permeated water (L), A is the effective area of the membrane (m^2), Δt is the permeation time (h), and C_p and C_f are the concentration in the permeate and feed (g/L), respectively. The solute concentration of active dyes was measured by a UV-Vis spectrophotometer (Shimadzu, Japan). The concentration of saline solution was measured with an electrical conductivity meter (DDS-11A, Shanghai Hongyi Instrument Co. Ltd, China).

Antifouling performance measurement

The antifouling performance of NF membranes was investigated with BSA (1 g/L) solution (PBS, 0.1 mol/L and pH 7.0) at 25°C and 0.4 MPa. In a typical procedure, pure water was first filtered through the membrane, rendering the system stable before use. Then pure water filtrated through the membrane for 100 min and the average water flux was recorded as $J_{w,1}$. The filtration of the BSA solution was continued for another 100 min and the flux of BSA was recorded as J_p. After that, the membrane was washed thoroughly with deionized water for 30 min (the washing time was not counted in the filtration cycle). The water flux of the cleaned membranes $J_{w,2}$ was measured again. The antifouling performance evaluation for each membrane was measured during 3 cycles. In order to evaluate the antifouling property of the membranes, the flux recovery ratio (*FRR*) and the total fouling ratio (R_t) were calculated by the following equation:

$$FRR = \frac{J_{w,2}}{J_{w,1}} \times 100\% \quad (5)$$

In order to analyze the fouling process in detail, total fouling ratio (R_t) is the degree of total flux decline caused by total fouling. Reversible fouling describes the fouling caused by concentration polarization and irreversible fouling is ascribed by adsorption or deposition of protein molecules. Reversible fouling ratio (R_r) and irreversible fouling ratio (R_{ir}) were calculated using the following equations:

$$R_t(\%) = (1 - \frac{J_p}{J_{w,1}}) \times 100\% \quad (6)$$

$$R_r(\%) = (\frac{J_{w,2} - J_p}{J_{w,1}}) \times 100\% \quad (7)$$

$$R_{ir}(\%) = (\frac{J_{w,1} - J_{w,2}}{J_{w,1}}) \times 100\% = R_t - R_r \quad (8)$$

Mechanical property

The tensile strength and elongation were measured on testing strips using a model UTM2203 electronic universal testing machine (Jinan Huike Test Instrument Co., Ltd., China) mounted with a 100 N load cell at room temperature at a constant crosshead speed of 5 mm/min with aluminum sample holder. Rectangle shapes of the samples (40 mm length and 10 mm width) were prepared and the thickness of all the membranes were obtained from the SEM results of membranes. Particular attention was given to the macroscopic homogeneity of membranes and only apparently homogeneous membranes were used for the mechanical tests.

Results and discussion

Characterization of GO-PSBMA nanocomposites

TEM images of GO (a, a') and GO-PSBMA (b, b') in different magnification are presented in Fig. 2 (A). As seen from Fig. 2(A) (a, a'), GO has a thin and laminar structure, and its size ranges from tens to several hundreds of square nanometers. It can be seen that the surface of GO was relatively smooth and no other impurities appeared. In contrast, modified GO became wrinkled and folded in the same condition of sample preparation. A large amount of irregular viscous precipitation (dark dots) are attached to the surface of the GO, rendering more darkish and rougher than pristine GO, which demonstrates that polymer brushes were smoothly grafted onto GO surface *via* RATRP.

X-ray diffraction (XRD) patterns provide insight into the exfoliated structure of GO. Fig. 2 (B) displays XRD patterns of GO, GO-Br, GO-PSBMA. GO has a fairly narrow and strong diffraction peak at 9.6°, indicating that the interlayer spacing of GO is 0.93 nm, which is similar to a related reference[41]. However, the diffraction angle of 10.1° for GO-Br showed that the interlayer distance decreased to 0.88 nm due to reduced intercalated water molecules between layers caused by decreasing oxygen containing functional groups. For GO-PSBMA, a relatively weak peak at 9° appears, corresponding to a interlayer distance of 0.97 nm induced by exerting the polymer brushes that can be seen in Fig. 2(A). Thus, the XRD patterns manifest a typical laminar structure of the graphene-based nanocomposites.

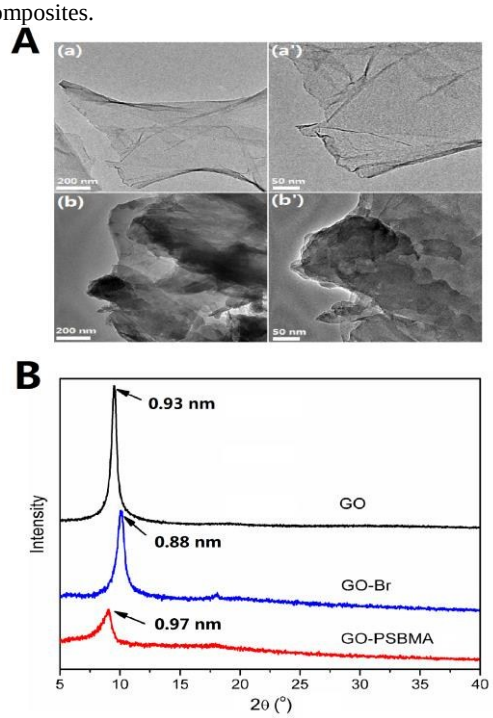

Fig. 2 (A) TEM images of GO (a, a') and GO-PSBMA (b, b') in different magnification, (B) XRD curves of (a) GO, (b) GO-Br and (c) GO-PSBMA

The synthesized GO, GO-Br, and GO-PSBMA were investigated by FT-IR; the results are shown in Fig. 3 (A). For GO, a wide peak around 3440 cm^{-1} was attributed to the O-H stretching vibration of GO and water. The curve of GO shows a stretching vibration of C=O at 1720 cm^{-1}, and two absorption peaks at 1230 cm^{-1} and 1040 cm^{-1} were induced by C-O and C-O-C vibration[54]. For GO-Br, the peak around 2930 cm^{-1} was assigned to the stretching vibration of C-H bonds in methyl or methylene groups of BTPAm. The adsorption peaks at 3440 cm^{-1} and 789 cm^{-1} correspond to the presence of N-H. Compared to GO, two new peaks at 1540 cm^{-1} and 1110 cm^{-1} representing C-N bonds and Si-O-Si bonds indicate that GO-Br was successfully synthesized[55]. Additionally, the peak at 1720 cm^{-1} obviously weakened and the peak at 1040 cm^{-1} disappeared, which demonstrates that GO was reduced to a certain degree. After the grafting of PSBMA, characteristic peaks at 1110 cm^{-1} and 1040 cm^{-1}

originating from symmetric and asymmetric stretching of O=S=O from sulfonate groups of grafted polymer[56] can be observed. The peak at 1720 cm^{-1} reinforces again, which demonstrates the C=O stretching vibration from PSBMA. Therefore, the polymerization of SBMA monomer onto the surfaces of GO via RATRP was favorably conducted.

Thermogravimetric analysis (TGA) is a useful technique to determine the composition and thermal stability of materials. In order to further confirm the modification of GO, Fig. 3 (B) presents the TGA curves of GO, GO-Br and GO-PSBMA obtained under a nitrogen atmosphere. The curve of GO with a major weight loss around 200°C was probably due to outgassing of labile functional groups, which leads to CO, CO_2 and steam release[19]. A slower mass loss between 400°C and 700°C was attributed to the thermal decomposition of more stable functional groups. However, a different decomposition pattern was observed both in GO-Br and GO-PSBMA. This may be explained by the loss of oxygen-containing functional groups during the silanization of GO, which was certified by the FT-IR results. GO-Br had a total weight loss of ca. 46.4 wt.% from room temperature to 700°C. The GO-PSBMA had a total weight loss of ca. 56.7 wt.%, indicating that the weight percent of PSBMA in GO-PSBMA is at least 10.3 wt.%. In overall, decomposition temperature of GO is lower than modified GO, indicating a certain increase of thermal stability of modified GO due to the decrease of oxygen-containing functional groups.

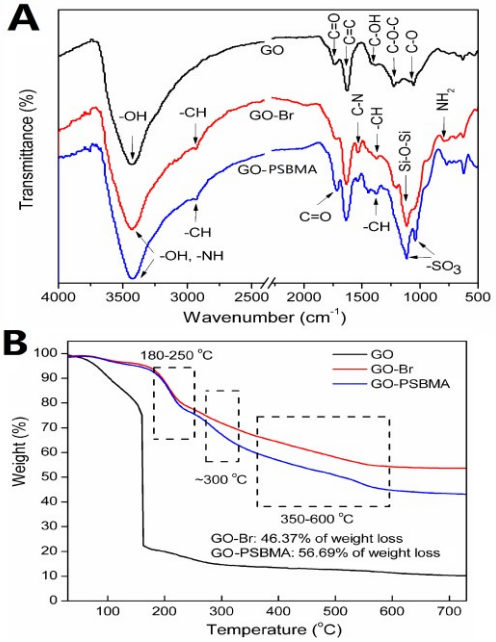

Fig. 3 (A) FTIR spectra of GO, GO-Br and GO-PSBMA, (B) TGA curves of GO, GO-Br and GO-PSBMA

Fig. S4 presents XPS survey spectra of GO and GO-PSBMA. For GO, there were only two major emissions involving C1s (284.6 eV) and O1s (532.0 eV). After grafting zwitterionic polymer bushes, several new characteristic peaks appeared, including Br 3s (255.2 eV), Br 3p (182.2 eV) and Br 3d (69.0 eV) which corresponded to initiator. The emission peaks at 165.8 eV (S 2p) and 400.8 eV (N 1s) confirmed the polymerization of SBMA onto GO surface in the RATRP process.

Characterization of PES/GO-PSBMA composite membranes

Morphology of the membrane

The cross-sectional SEM images of pristine membranes and hybrid membranes with different GO-PSBMA content are shown in Fig. 4. All membranes prepared by phase inversion have a typical thin active layer and a finger-like support layer. No apparent difference was observed in cross-sectional structure between pristine and hybrid membranes. Fig. S5 (A-D) presented a magnified cross-sectional images of all prepared membranes. The thickness of the skin layer of NFM-0, NFM-1, NFM-2 and NFM-3 marked in this figure is ca. 0.468, 0.429, 0.794 and 0.543 μm, respectively. The tendency of the thickness affected by mixing with nanocomposites has been reported by similar work[27]. A decline in the thickness of NFM-1 was due to the hydrophilic GO-PSBMA which can accelerate water (non-solvent) inflow during phase inversion, forming a relative thin top layer[36]. Nonetheless, a further increase of nanocomposites enhanced the viscosity of dope solution, which decreases the mass transfer rate of non-solvent, thus giving rise to an enhanced thickness of skin layer. In addition, the existence of inorganic section from hybrid composites among casting solution will impair the interaction of PES chain, and hydrophilic GO-PSBMA also could accelerate water (non-solvent) inflow, thus forming a relatively loose skin layer. As shown in Fig. 4 (a'-d'), when the content of GO-PSBMA composites increased to 0.44%, the macrovoids decreased and the connectivity of the holes was suppressed due to the increased viscosity ascribed to the GO-PSBMA composites and hydrogen bonds formed between GO-PSBMA and DMAc. In summary, two factors (hydrophilicity and viscosity) dominated the membrane structure in opposite directions, forming a porous and loose hybrid membrane.

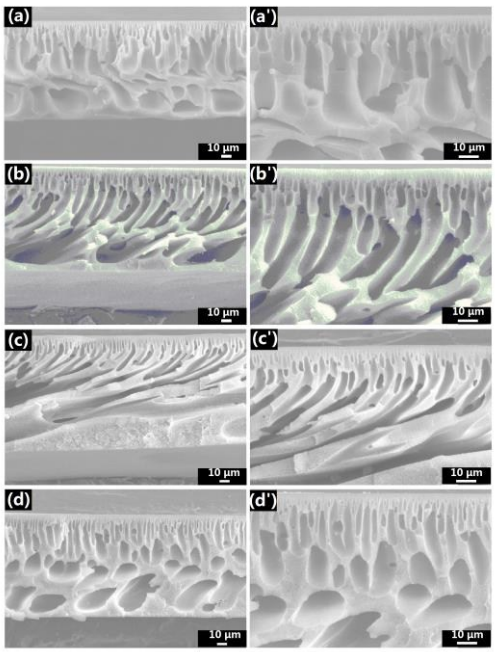

Fig. 4 Cross-section morphologies of GO-PSBMA/PES hybrid membranes: (a, a') NFM-0, (b, b') NFM-1, (c, c') NFM-2, (d, d') NFM-3

Hydrophilicity of membrane

Surface hydrophilicity of prepared membranes was characterized by water contact angle measurement. A hydrophilic membrane surface is prone to the formation of a tight and compact water layer adjacent to the surface, which reduces the deposition and adsorption of hydrophobic foulants. The water contact angle are plotted in Fig. 5 (B). It was observed that the initial contact angle and that after 60 seconds of NFM-0 was 84°, 76.8°, respectively, which manifests a slower tendency for surface wettability. The initial contact angle of NFM-2 decreases to 54.8° when the GO-PSBMA content was 0.22 wt.%, demonstrating a significant increase of surface hydrophilicity.

This is assumed to be related to hydrophilic GO-PSBMA migrating toward the top layer during phase inversion, giving rise to the lower water contact angles. This can be confirmed by Fig. 5 (A), showing that the hybrid membrane surface was darker than NFM-0 due to the incorporation of GO-PSBMA nanoplates. Besides, pristine membrane and NFM-3 are investigated by using XPS analysis and survey spectra are shown in Fig. S6. Compared with unmodified PES membrane, the intensity of peaks corresponding S2p and N1s greatly enhanced, along with new peaks (Si2p) appearing, thus notably confirming the exsitence of GO-SBMA nanoplates onto membrane surface. However, the water contact angle of NFM-3 was again higher than that of NFM-2. This is thought to be due to the combination of an increase of hydrophobic organic chains and partial agglomeration of GO-PSBMA composites. In summary, the hybrid membranes exhibited a better hydrophilicity than pristine PES membrane due to the addition of GO-PSBMA nanoplates.

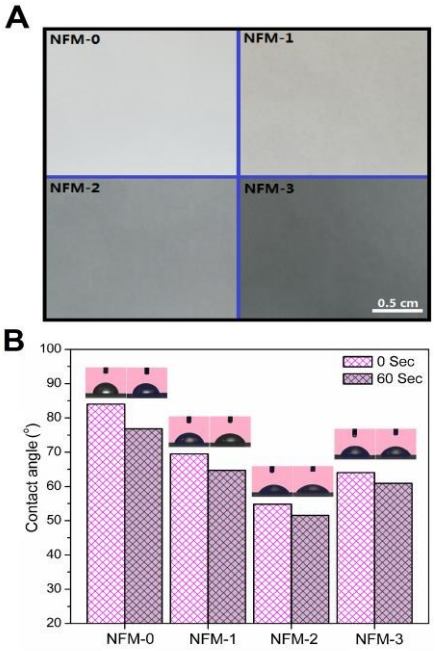

Fig. 5 (A) Top surface photos of hybrid membrane with different GO-PSBMA content, (B) Effect of GO-PSBMA content on water contact angle of hybrid membranes

Water permeability of membrane

The water uptake (inset) and pure water flux of each prepared membrane are plotted in Fig. 6. Generally, the water uptake and water permeability is mainly related to hydrophilicity and the loose structure of composite membranes. It was found that the pure water flux markedly enhanced with the incorporation of GO-PSBMA composites, which was consistent with the results of water uptake and contact angle. Specifically, at 0.6 MPa, NFM-0 has the lowest water uptake (120.5%) and pure water flux (38.6 L m^{-2} h^{-1}), whereas the corresponding value of NFM-2 signally increased to 202.3% and 71.7 L m^{-2} h^{-1}, respectively. This indeed corresponds to the improved hydrophilicity, loose skin layer and more porous macro-voids. It was obviously found that the addtion of GO-PSBMA substantially enhanced the loose degree of hybrid membranes in view of the overall porosity of membranes (Fig. S7). In addition, sufficient GO-PSBMA nanoplates present in the polymer matrix can reduce the interaction of the polymer chains and undermine the polymer chain packing to a certain degree due to their inorganic constituent, thereby decreasing compactness and density of skin layer, but in another sense promoting the water permeability and water uptake. However, with a further increase of the GO-PSBMA content (0.44 wt.%), both water uptake and water permeability reduced compared with NMF-2. A plausible explanation is that GO blocks pathways for permeation, and may also partially agglomerate. This would decrease the effective membrane area. Additionally, the decline in hydrophilicity of membrane surface further enhances this effect. In conclusion, the loose NF membrane presented a substantial increase both in pure water flux and water uptake in comparison with pristine PES membrane.

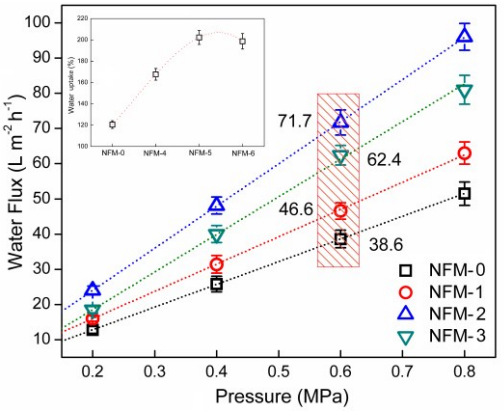

Fig. 6 Pure water flux and water uptake (inert) of hybrid GO-PSBMA/PES membranes

Surface charge of membranes

Surface charge is a vital parameter that affects the separation properties of NF membranes, especially for separating charged solutes and salts. In this work, the zeta potential was measured to investigate the surface charge of NF membranes (see Fig. 7). The pristine membrane (NFM-0) has a negative zeta potential in a wide range of pH values. In the pH range from 6 to 10, the zeta potential followed the following order: NMF-0 < NMF-3 < NMF-2 < NMF-1. Thus, the charge density on the surface of hybrid membrane was higher with an incorporation of GO-PSBMA composites. However, the charge density becomes increasingly lower with an increase of the GO-PSBMA content. A possible explanation is that GO is negatively charged, whereas PSBMA is electrically neutral. Polymer brushes are available to cover GO surface in a range of scopes, reducing the negative charge density of GO-PSBMA composites. A lower negative charge may be due to the incorporation of polymer brushes. Overall, the zeta potential measurements demonstrate that the surface of the membranes was negatively charged.

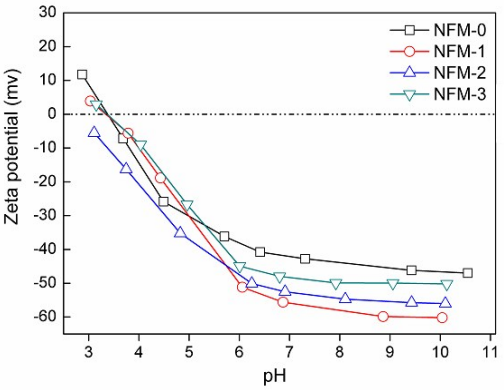

Fig. 7 Zeta potentials of (a) NFM-0, (b) NFM-1, (c) NFM-2 and (d) NFM-3 at different pH

Separation property of membrane

Two types of dye solution, Reactive Red 49 (RR49) and Reactive Black 5 (RB5), were applied to explore the NF performance of the prepared membranes. Fig. 8 (A) shows the effect of the content of incorporated GO-PSBMA on the rejection and permeation flux of dyes for NF membranes. The hybrid membranes have a high

rejection of RR49 (>92%) and RB5 (>97.5%) due to the incorporation of GO-PSBMA composites. Furthermore, the rejection of RR49 and RB5 continuously rose with the increasing GO-PSBMA content. When the content of GO-PSBMA composites was 0.22 wt.%, the rejection of RB5 was as high as 99.2%, which increased by 7.8% in contrast with that of pristine membrane. The improved retention suggests that the introduction of GO-PSBMA results in a lower compactness and density of the top layer, which had no significant impact on the rejection performance of hybrid membranes. In addition, the combination of increased charge density and GO blocking of permeation pathways endowed the hybrid membranes with high level of rejection for RR49 and RB5. In order to investigate the potential for treatment of dye solutions, the permeation flux of RR49 and RB5 was measured. As shown in Fig. 9, the tendency of dyes permeation was consistent with the pure water flux. Specifically, the permeation flux reached 37.5 kg m^{-2} h^{-1} for NFM-2 at 0.4 MPa, whereas NFM-0 had the lowest flux of 14.9 kg m^{-2} h^{-1}. As previously mentioned, the improved permeation flux mainly originates from the combination of a loose top layer, the porous structure, and higher surface hydrophilicity of hybrid membrane .

Salt rejection influenced by the content of GO-PSBMA nanoplates is shown in Fig. 8 (B). The salt rejection of hybrid membranes followed the order Na_2SO_4 > $MgSO_4$ > NaCl > $MgCl_2$, demonstrating that the hybrid membranes were negatively charged, which is consistent with the zeta potential results. It is also apparent that the salt rejection of hybrid membranes decreases with the content of GO-PSBMA composites. Specifically, for NFM-3, the rejection of bivalent salts including Na_2SO_4, $MgCl_2$ and $MgSO_4$ decreases to 9.0%, 2.56% and 8.51%, respectively.

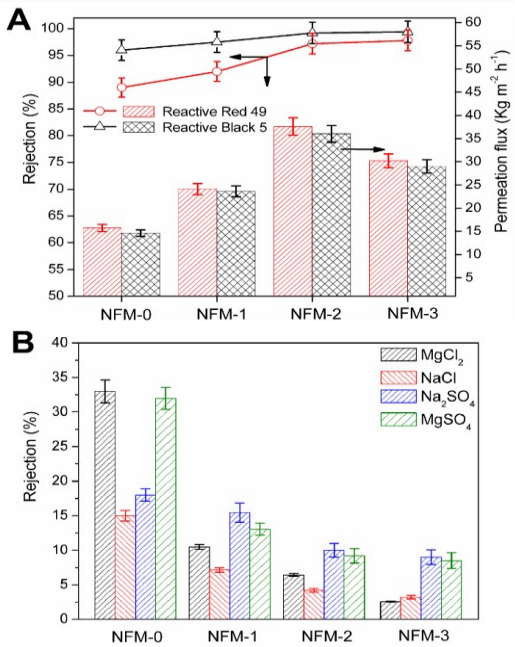

Fig. 8 (A) Permeation flux and rejection of dyes (Reactive Red 49, Reactive Black 5), (B) Effect of GO-PSBMA content on rejection of mono- and bi-valent salts

The decline tendency of salt rejection was different with the work as reported by our previous work[27]. Due to an improved charge density of chitosan-montmorillonite/PES (CS-MMT/PES) hybrid membranes compared with pristine membrane, Na_2SO_4 rejection remained a continuous growth trend for hybrid membranes with enhacing the CS-MMT content. In this work, cnversely, salt rejection exhibited a sustained downward trend with an increase of PSBMA content. This may be due to electrostatic interaction induced by GO-PSBMA composites. The grafting of PSBMA, whose polar groups comprise alternating quaternary ammonium groups (positively charged) and sulfonic groups (negatively charged), forming an easier passage of anions and cations in the skin layer and therefore could facilitate salts permeation through the hybrid membranes (as shown in Fig. 9). Additinally, GO-PSBMA/PES membrane presented a higher rejection of reactive dyes compared with CS-MMT membranes, indicating that Overall, the loose structure of the skin layer and charged surface plays a crucial role in the separation properties of the hybrid membranes, leading to higher retention of reactive dyes and salt transmission compared to pristine membranes. These results indicate that loose NF membranes have potential for the fractionation of dye/salt mixture.

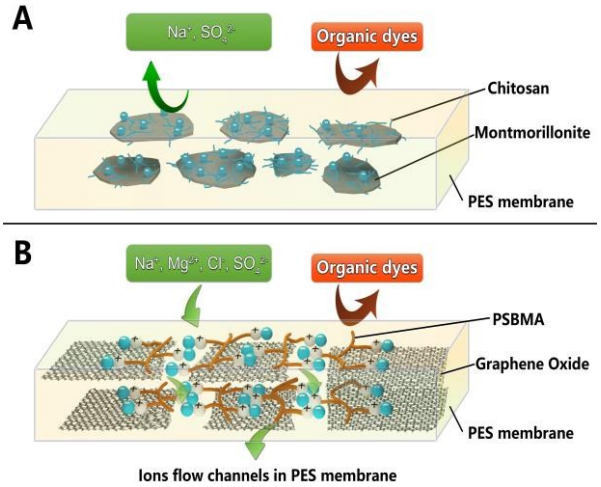

Fig. 9 Schematic illustration of salts permeation for hybrid membranes (A) CS-MMT/PES membrane, (B) GO-PSBMA/PES membrane

In order to investigate membrane stability, a short-time of filtration experiment was performed. Fig. 10 displays the retention and permeation flux of reactive dyes (RR49 and RB5) during 60 h of filtration. It was found that both RR49 and RB5 exhibited a certain amount of decline in permeation flux, along with a slight increase of dyes rejection. This may be attributed to two factors, namely cake-enhanced concentration polarization (CECP) and the formation of a dye cake layer, which deteriorated the flux of NF membranes with a synergic effect[29]. But in this case, due to a good water solubility of reactive dyes, the adsorption process may be dynamic and then the filtration process can keep stable once equilibrium is established.

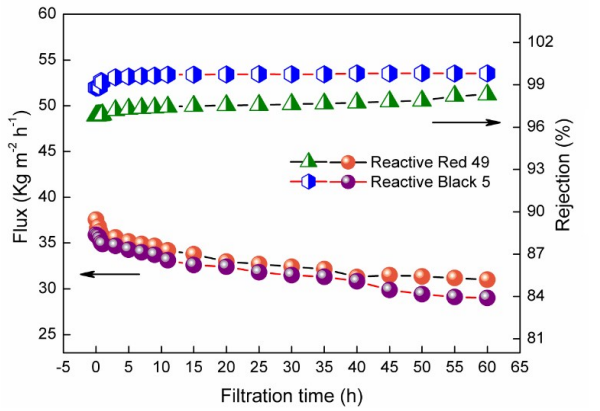

Fig.10 Short-time stability test of NFM-2 (0.4 MPa, 500 mg/L, 25±1 °C).

Antifouling performance of membrane

The process of membrane fouling is very complicated; fouling induced by protein adsorption derives from the combination of electrostatic interaction, hydrogen bonding, hydrophobic impact and van der Waals forces. Ostuni *et al*.[57] reported that an ideal membrane surface which is immune to protein fouling should have the following features: good hydrophilicity, containing hydrogen bond receptors, free from hydrogen bond donors, and overall electric neutrality. Therefore, in this work, zwitterionic polymer (PSBMA) was grafted onto GO since it contains phosphatidylcholine, which conforms to these requirements. It may be assumed that zwitterionic polymers have an excellent antifouling property. To investigate the antifouling of prepared membranes, a BSA solution (pH=7) was chosen as a model protein. The isoelectric point of BSA (IEP_{BSA}) is about 4.9, hence, BSA was negatively charged.

Fig. 11 (A) presents the permeation flux of tested membranes before and after protein filtration. The water flux of the fouled membranes was measured, followed by filtration of deionized water for 30 min. The permeation flux of the prepared membranes markedly decreases when deionized water was replaced by the BSA solution. The decline of permeation was mainly due to concentration polarization and membrane fouling. Subsequently, the permeation flux recovered to varying degrees and remained subtle floating after rinsing with pure water. Finally, the flux recovery was measured to investigate the antifouling performance of the prepared membranes. The results of total flux decline ratio (R_t) and flux recovery ratio (*FRR*) of loose NF membranes are shown in Fig. 11 (B). The pristine membrane (NFM-0) has the lowest *FRR* (56.5%), whereas the R_t was as high as 59.6%. A higher *FRR* and lower R_t represent a better antifouling property for the membrane. With the incorporation of GO-PSBMA composites, the overall *FFR* of hybrid membranes was over 70% and the R_t markedly decreases compared with pristine membranes. More specifically, the *FRR* of NFM-2 was as high as 95.4%, and the irreversible fouling ratio (R_{ir}) considerably reduced from 43.5% for NFM-0 to 5.6% for NFM-2. In irreversible fouling, the foulants are tightly attached to the membrane and are difficult to be removed by facile washing. The results show that NFM-2 has an excellent antifouling property. However, with a further increase of GO-PSBMA composites (0.44 wt.%), the *FRR* value of NFM-3 reduces to 89.2%, and the irreversible fouling ratio (R_{ir}) increases to 13.7% in comparison with NFM-2. This may be explained by hydrophobic chains deriving from GO-PSBMA and partial agglomeration, which is consistent with the water contact angle results. In addition, charge density differences between NFM-2 and NFM-3, which gave rise to the lower electrostatic repulsion against negatively charged BSA, also play a role in the lower antifouling properties of NFM-3. In addition to surface hydrophilicity, surface roughness is another crucial factor which has a significant effect on antifouling property of the membrane. Hence, with the purpose of further evaluating the surface roughness of membranes, AFM images and roughness analysis were performed. As shown in Fig. S8, pristine membrane displayed more bumps with higher height compared with that of NFM-3. Roughness average (Ra) of NFM-0 was 17.496 nm and root mean square (Rms) was 13 nm, whereas the values of NFM-2 greatly reduced to 3.101 nm and 2.419 nm, respectively. Such results demonstrated that the improved antifouling property of hybrid membranes benefited from low surface roughness to a certain extent.

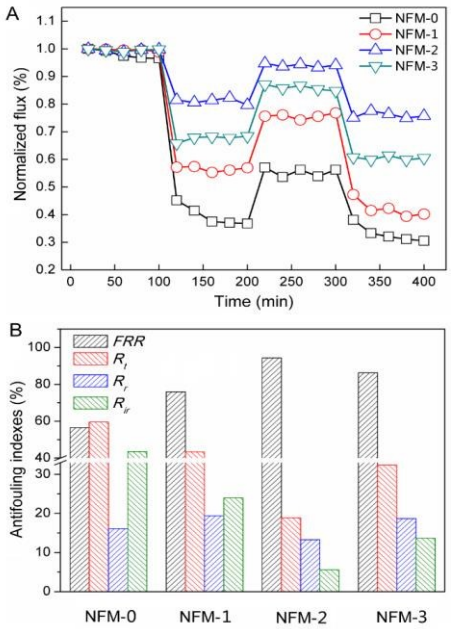

Fig. 11 (A) Normalized flux of hybrid membrane before and after the filtration of BSA solution, (B) Fouling resistance ratio of pristine and hybrid membranes

Mechanical properties of membrane

Fig. 12 shows the mechanical stability of pristine and hybrid membranes in terms of their stress-strain curves. The pristine membrane has a relatively common mechanical stability, i.e., a tensile strength of 3.2 MPa and an elongation at break of about 13.7%. When incorporating GO-PSBMA nanoplates into PES matrix, the hybrid membrane has a substantially improved mechanical strength in comparison with the pristine membrane. By elevating the GO-PSBMA content from 0.11 wt.% to 0.44 wt.% the tensile strength increases from 4.5 to 5.6 MPa. Such an improvement of the hybrid membranes is partially attributed to the formation of an intercalated structure, which limits the chain mobility of PES matrix to a certain extent. Hence, the hybrid membrane has improved mechanical properties. Additionally, GO-PSBMA obtained by organic modification of GO has a good dispersion and interface compatibility in PES, having little or no influence on the homogeneity of hybrid membranes. Thus, the combination of the stiffness of the inorganic material and the flexibility of the polymeric material effectively improves the mechanical stability of the PES matrix, which makes these hybrid membranes promising for nanofiltration application.

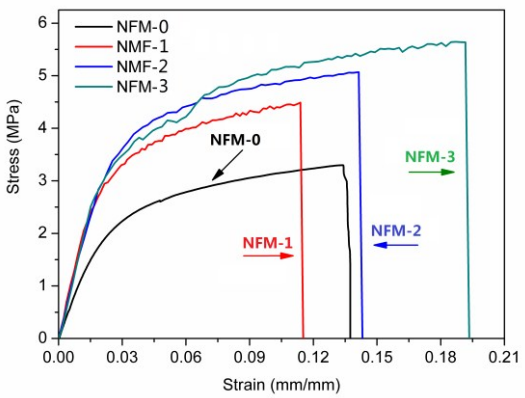

Fig. 12 Effect of GO-PSBMA content on mechanical property of pristine and hybrid membranes

Conclusion

Graphene oxide was synthesized and subsequent surface zwitterionization of GO was successfully conducted *via* RATRP. The hybrid membranes were prepared by mixing GO-PSBMA nanoplates with the polymeric matrix *via* phase inversion. Characterization of GO-PSBMA composites by FT-IR, TGA, TEM, and XRD demonstrates that GO nanosheets were well modified. The influence of GO-PSBMA composites on the morphology, hydrophilicity, mechanical properties, permeation and antifouling performance of hybrid membranes were investigated. The main conclusions of this work can be drawn as follows: The water permeability of hybrid membranes reaches up to 11.98 L m^{-2} h^{-1} bar^{-1}, which is due to the combination of a loose and porous structure and a high hydrophilicity; It was observed that by increasing the GO-PSBMA content from 0 to 0.22 wt.% the R_{ir} reduced from 43.5% to 5.6% for NFM-2, demonstrating an excellent antifouling performance; The novel membranes have the high retention of LMW dyes and salts permeation, and improved mechanical strength, showing a potential for the fractionation of dye/salt mixture in textile wastewater.

Acknowledgements

This work was supported by National Natural Science Foundation of China (Nos. 21476215 and 21376225).

Notes and references

[a] School of Chemical Engineering and Energy, Zhengzhou University, Zhengzhou 450001, P. R. China
[b] UNESCO Centre for Membrane Science and Technology, School of Chemical Engineering, University of New South Wales, Sydney, NSW 2052, Australia
[c] Department of Chemical Engineering, KU Leuven, Willem de Croylaan 46, B-3001 Heverlee, Belgium
E-mail: zhangyatao@zzu.edu.cn

1. J. Wu, J. Wang, H. Li, Y. Du, K. Huang and B. Liu, *J. Mater. Chem. A*, 2013, **1**, 9837-9847.
2. J. Zhu, Y. Zhang, M. Tian and J. Liu, *ACS Sustainable Chem. Eng.*, 2015, **3**, 690-701.
3. A. Gopalakrishnan, M. L. Mathew, J. Chandran, J. Winglee, A. R. Badireddy, M. Wiesner, C. T. Aravindakumar and U. K. Aravind, *ACS Appl. Mater. Interfaces*, 2015, **7**, 3699-3707.
4. S. Guan, S. Zhang, R. Han, B. Zhang and X. Jian, *Desalination*, 2013, **318**, 56-63.
5. S. Yu, C. Gao, H. Su and M. Liu, *Desalination*, 2001, **140**, 97-100.
6. J. Luo and Y. Wan, *J. Membr. Sci.*, 2011, **372**, 145-153.
7. M. Xie and Y. Xu, *J Hazard. Mater.*, 2011, **186**, 960-964.
8. Q. Chen, P. Yu, W. Huang, S. Yu, M. Liu and C. Gao, *J. Membr. Sci.*, 2015, **492**, 312-321.
9. N. Ghaemi, S. S. Madaeni, P. Daraei, H. Rajabi, T. Shojaeimehr, F. Rahimpour and B. Shirvani, *J. Hazard. Mater.*, 2015, **298**, 111-121.
10. R. Bernstein, E. Anton and M. Ulbricht, *ACS Appl. Mater. Interfaces*, 2012, **4**, 3438-3446.
11. J. Zhu, N. Guo, Y. Zhang, L. Yu and J. Liu, *J. Membr. Sci.*, 2014, **465**, 91-99.
12. Y. Li, Y. Su, X. Zhao, X. He, R. Zhang, J. Zhao, X. Fan and Z. Jiang, *ACS Appl. Mater. Interfaces*, 2014, **6**, 5548-5557.
13. A. W. Mohammad, Y. H. Teow, W. L. Ang, Y. T. Chung, D. L. Oatley-Radcliffe and N. Hilal, *Desalination*, 2015, **356**, 226-254.
14. A. K. Singh, S. Prakash, V. Kulshrestha and V. K. Shahi, *ACS Appl. Mater. Interfaces*, 2012, **4**, 1683-1692.
15. J. Lin, W. Ye, H. Zeng, H. Yang, J. Shen, S. Darvishmanesh, P. Luis, A. Sotto and B. Van der Bruggen, *J. Membr. Sci.*, 2015, **477**, 183-193.
16. L. Yu, Y. Zhang, Y. Wang, H. Zhang and J. Liu, *J Hazard. Mater.*, 2015, **287**, 373-383.
17. C. Zhao, J. Xue, F. Ran and S. Sun, *Prog. Mater. Sci.*, 2013, **58**, 76-150.
18. V. Vatanpour, M. Esmaeili and M. H. D. A. Farahani, *J. Membr. Sci.*, 2014, **466**, 70-81.
19. L. Yu, Y. Zhang, B. Zhang, J. Liu, H. Zhang and C. Song, *J. Membr. Sci.*, 2013, **447**, 452-462.
20. H. Yu, X. Zhang, Y. Zhang, J. Liu and H. Zhang, *Desalination*, 2013, **326**, 69-76.
21. H. Yu, Y. Zhang, X. Sun, J. Liu and H. Zhang, *Chem. Eng. J.*, 2014, **237**, 322-328.
22. X. Fan, Y. Dong, Y. Su, X. Zhao, Y. Li, J. Liu and Z. Jiang, *J. Membr. Sci.*, 2014, **452**, 90-96.
23. Q.-F. An, W.-D. Sun, Q. Zhao, Y.-L. Ji and C.-J. Gao, *J. Membr. Sci.*, 2013, **431**, 171-179.
24. W. Fang, L. Shi and R. Wang, *J. Membr. Sci.*, 2013, **430**, 129-139.
25. B. Van der Bruggen, B. Daems, D. Wilms and C. Vandecasteele, *Sep. Purif. Technol.*, 2001, **22-23**, 519-528.
26. L. Yu, Y. Zhang, H. Zhang and J. Liu, *Desalination*, 2015, **359**, 176-185.
27. J. Zhu, M. Tian, Y. Zhang, H. Zhang and J. Liu, *Chem. Eng. J.*, 2015, **265**, 184-193.
28. L. Xing, N. Guo, Y. Zhang, H. Zhang and J. Liu, *Sep. Purif. Technol.*, 2015, **146**, 50-59.
29. J. Lin, C. Y. Tang, W. Ye, S.-P. Sun, S. H. Hamdan, A. Volodin, C. V. Haesendonck, A. Sotto, P. Luis and B. Van der Bruggen, *Journal of Membrane Science*, 2015, **493**, 690-702.
30. H. Deng, Y. Xu, Q. Chen, X. Wei and B. Zhu, *J. Membr. Sci.*, 2011, **366**, 363-372.
31. T. He, M. Frank, M. H. V. Mulder and M. Wessling, *J. Membr. Sci.*, 2008, **307**, 62-72.
32. T. Puspasari, N. Pradeep and K.-V. Peinemann, *J. Membr. Sci.*, 2015, **491**, 132-137.
33. J. Campbella, R. P. Davies, C. Braddock and A. G. Livingston, *J. Mater. Chem. A*, 2015, **3**, 9668-9674.
34. V. Vatanpour, S. S. Madaeni, R. Moradian, S. Zinadini and B. Astinchap, *J. Membr. Sci.*, 2011, **375**, 284-294.
35. V. Vatanpour, S. S. Madaeni, R. Moradian, S. Zinadini and B. Astinchap, *Sep. Purif. Technol.*, 2012, **90**, 69-82.
36. N. Ghaemi, S. S. Madaeni, A. Alizadeh, H. Rajabi and P. Daraei, *J. Membr. Sci.*, 2011, **382**, 135-147.
37. J. Zhang, Y. Zhang, Y. Chen, L. Du, B. Zhang, H. Zhang, J. Liu and K. Wang, *Ind. Eng. Chem. Res.* , 2012, **51**, 3081-3090.
38. K. P. Loh, Q. Bao, G. Eda and M. Chhowalla, *Nat. Chem.*, 2010, **2**, 1015-1024.
39. J. Liu, J. Tang and J. J. Gooding, *J. Mater. Chem.*, 2012, **22**, 12435-12452.
40. K. Cao, Z. Jiang, J. Zhao, C. Zhao, C. Gao, F. Pan, B. Wang, X. Cao and J. Yang, *J. Membr. Sci.*, 2014, **469**, 272-283.
41. K. Goh, L. Setiawan, L. Wei, R. Si, A. G. Fane, R. Wang and Y. Chen, *J. Membr. Sci.*, 2015, **474**, 244-253.
42. Y. P. Tang, J. X. Chan, T. S. Chung, M. Weber, C. Staudt and C. Maletzko, *J. Mater. Chem. A*, 2015, **3**, 10573-10584.
43. J. Wang, X. Gao, J. Wang, Y. Wei, Z. Li and C. Gao, *ACS Appl. Mater. Interfaces*, 2015, **7**, 4381-4389.
44. Y. F. Zhao, P. B. Zhang, J. Sun, C. J. Liu, Z. Yi, L. P. Zhu and Y. Y. Xu, *J. Colloid. Interface. Sci.*, 2015, **448**, 380-388.
45. Y.-F. Mi, Q. Zhao, Y.-L. Ji, Q.-F. An and C.-J. Gao, *J. Membr. Sci.*, 2015, **490**, 311-320.
46. P. Wang, J. Meng, M. Xu, T. Yuan, N. Yang, T. Sun, Y. Zhang, X. Feng and B. Cheng, *J. Membr. Sci.*, 2015, **492**, 547-558.
47. Y.-L. Ji, Q.-F. An, Q. Zhao, W.-D. Sun, K.-R. Lee, H.-L. Chen and C.-J. Gao, *J. Membr. Sci.*, 2012, **390-391**, 243-253.
48. G. Ye, J. Lee, F. Perreault, M. Elimelech, *ACS Appl. Mater. Interfaces*, 2015, **7**, 23069−23079.
49. T.Y. Liu, H.G. Yuan, Q. Li, Y. H. Tang, Q. Zhang, W. Qian, B. Van der Bruggen, X. Wang, *ACS Nano*, 2015, **9**, 7488–7496.
50. D. C. Marcano, D. V. Kosynkin, J. M. Berlin, A. Sinitskii, Z. Sun, A. Slesarev, L. B. Alemany, W. Lu and J. M. Tour, *ACS Nano*, 2010, **4**, 4806-4814.
51. H. P. Xu, W. Z. Lang, X. Yan, X. Zhang, Y. J. Guo, J. Membr. Sci., 2014, **467**, 142-152.

52. Z. Cui, N. T. Hassankiadeh, S. Y. Lee, J. M. Lee, K. T. Woo, A. Sanguineti, V. Arcella, Y. M. Lee, E. Drioli, *J. Membr. Sci.*, 2013, **444**, 223-236.
53. Y. Wang, J. Zhu, G. Dong, Y. Zhang, N. Guo and J. Liu, *Sep. Purif. Technol.*, 2015, **150**, 243-251.
54. Y. Lin, J. Jin and M. Song, *J. Mater. Chem.*, 2011, **21**, 3455-3461.
55. H. Roghani-Mamaqani, V. Haddadi-Asl, K. Khezri and M. Salami-Kalajahi, *RSC Advances*, 2014, **4**, 24439-24452.
56. X. Sun, W. Wang, T. Wu, H. Qiu, X. Wang and J. Gao, *Mater. Chem. Phys.*, 2013, **138**, 434-439.
57. E. Ostuni, R. G. Chapman, R. E. Holmlin, S. Takayama and G. M. Whitesides, *Langmuir* 2001, **17**, 5605-5620.

Graphical abstract